Synthesis, Structural, and Optical Properties in Monoclinic Er:KYb(WO 4) 2 Nanocrystals

5 AUTHORS, INCLUDING:

Montserrat Galceran
CIC Energigune
35 PUBLICATIONS **299** CITATIONS

SEE PROFILE

Maria Cinta Pujol
Universitat Rovira i Virgili
180 PUBLICATIONS **2,179** CITATIONS

SEE PROFILE

Carlos Zaldo
Spanish National Research Council
242 PUBLICATIONS **3,489** CITATIONS

SEE PROFILE

Synthesis, Structural, and Optical Properties in Monoclinic Er:KYb(WO$_4$)$_2$ Nanocrystals

M. Galceran,[†] M. C. Pujol,*,[†] C. Zaldo,[‡] F. Díaz,[†] and M. Aguiló[†]

Física i Cristal·lografia de Materials i Nanomaterials (FiCMA-FiCNA), Universitat Rovira i Virgili (URV), Campus Sescelades, c/ Marcel·lí Domingo, s/n, E-43007 Tarragona, Spain and Instituto de Ciencia de Materiales de Madrid (ICMM), Consejo Superior de Investigaciones Científicas (CSIC), c/Sor Juana Inés de la Cruz 3, E-28049 Cantoblanco, Madrid, Spain

Monoclinic-nondoped and erbium-doped KYb(WO$_4$)$_2$ nanocrystals around 50 nm were synthesized using the modified Pechini sol−gel method. Differential thermal and thermogravimetric analysis (DTA-TG) was used to study the thermal evolution of the precursor powder. X-ray powder diffraction (XRD) was used to confirm the presence of the monoclinic phase. We used electron microscopy techniques (SEM and TEM) to observe the morphology and particle size, and we estimated the particle size using Scherrer's equation. The optical spectroscopy of the trivalent ytterbium and erbium ions in monoclinic KYbW nanocrystals was studied by absorption and emission measurements at low and room temperature. The energy of the Stark sublevel of ytterbium and erbium in the ground- and excited-state KYbW nanocrystals has been determined. After exciting at 940 nm, the green photoluminescence ($^4S_{3/2} \rightarrow {}^4I_{15/2}$) and the 1.5 μm infrared ($^4I_{13/2} \rightarrow {}^4I_{15/2}$) emissions were observed because of the energy transfer from the ytterbium $^2F_{5/2}$ level to the $^4I_{11/2}$ erbium level. The decay times of Yb^{3+} ($^2F_{5/2}$) and Er^{3+} ($^4I_{13/2}$) excited levels were also studied at room temperature.

I. Introduction

Monoclinic potassium rare earth double tungstates, KRE-(WO$_4$)$_2$ (RE = rare earths, hereafter KREW), are excellent solid-state laser hosts for lanthanides. Lanthanide-doped KREW materials have large absorption and emission cross sections, and their anisotropy gives them special features. Lanthanide doping can reach stoichiometric active materials such as KREW (RE = Nd, Ho, Er, Tm, Dy, and Yb).[1−4] Continuous-wave laser action at 1 μm has already been achieved in KYb(WO$_4$)$_2$ (hereafter KYbW) crystal.[5,6] The present paper deals with KYbW and the erbium-doped KYbW (hereafter Er:KYbW). Spectroscopic studies of erbium doping in KYbW bulk single crystal can be found in work by Mateos et al.[7,8]

Ytterbium ion is an interesting alternative laser ion to neodymium in the 1 μm spectral region. Owing to its very simple energy level scheme (only one absorption band, $^2F_{7/2} \rightarrow {}^2F_{5/2}$). It has several advantages over neodymium, such as a small thermal loading due to a single de-excitation channel, no excited-state absorption or up-conversion losses, a large transparency over the visible range, a weaker cross-relaxation process, and a long (ms) radiative lifetime.[9−11] On the contrary, trivalent erbium has a rich energy level structure; therefore, it is used to obtain laser radiation at several wavelengths and, in particular, at 1.5 μm (corresponding to the $^4I_{13/2} \rightarrow {}^4I_{15/2}$ transition) of interest in telecommunications. However, its pumping by laser diodes around 980 nm is compromised by the low absorption cross section of the $^4I_{11/2}$ multiplet ($\sigma \approx 1 \times 10^{20}$ cm^2). Trivalent ytterbium acts as a good sensitizer ion for trivalent erbium because ytterbium has a high absorption cross section in this spectral range ($\sigma \approx 11 \times 10^{20}$ cm^2) and a good overlap exits between the $^4I_{11/2}$ and $^2F_{5/2}$ energy levels of erbium and ytterbium, respectively. The green emission in Er^{3+} ($^4S_{3/2} \rightarrow$
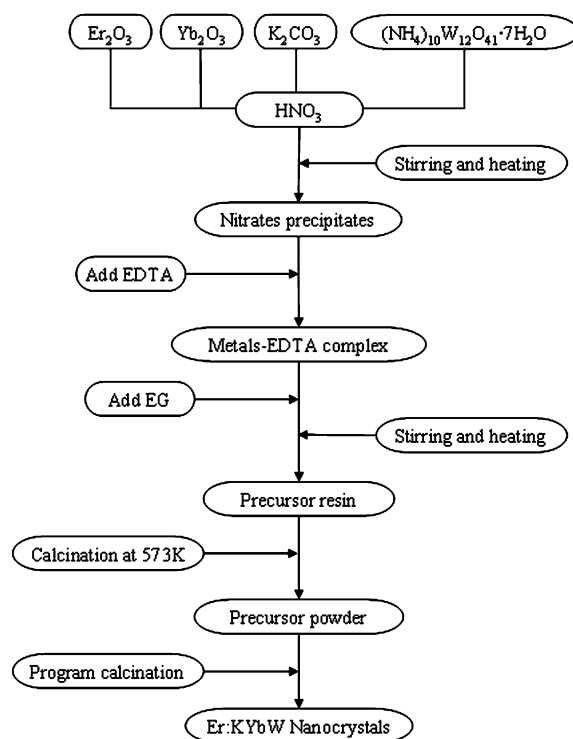

Figure 1. Schematic diagram of the nanocrystal preparation using the modified Pechini method.

$^4I_{15/2}$) is useful for color displays, high-density optical storage, biomedical diagnostics, sensors, and undersea optical communications. The $^4S_{3/2}$ level can be populated by up conversion after Yb−Er transfer.[12]

In recent years, there has been much interest in the study and synthesis of lanthanide-doped nanocrystals. These nanocrystals could be the first step for preparing nanoceramic laser material because of the enhancement of the sintering activity

---

* To whom correspondence should be addressed. Phone: +34 9775586286. Fax: +34 977559563. E-mail: mariacinta.pujol@urv.cat.
† Universitat Rovira i Virgili.
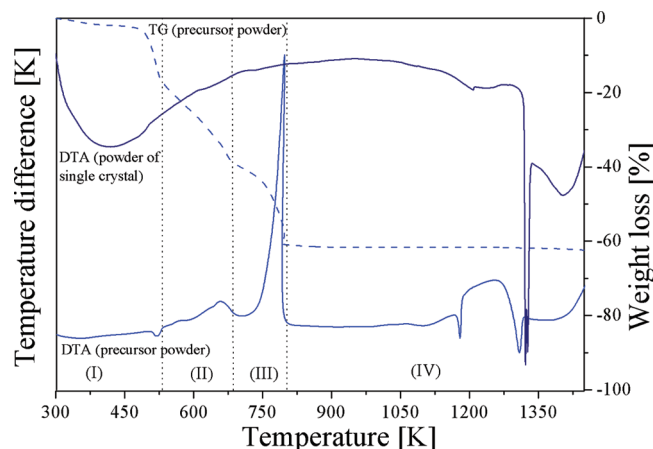‡ Consejo Superior de Investigaciones Científicas.

Figure 2. DTA-TG analysis of the precursor powder.

due to the nanometric size dimension.[13] Polycrystalline powders are less expensive and easier to obtain than single-crystal growth. Also, sintering the nanocrystals to form a ceramic can improve the thermal and mechanical properties of the active material. On the other hand, in some laser hosts such as YAG, it is possible to achieve a higher concentration of lanthanide elements in the nanocrystal rather than in the bulk single crystal.[14]

Because of their particle size, lanthanide-doped nanocrystals can have different spectroscopic properties compared to their bulk counterpart, such as a different emission lifetime, luminescence quantum efficiency, concentration quenching, etc.[15−18] These facts could be due to (a) a greater fraction of active ions being near the surface because of their volume to area ratio, (b) the disorder on the surface of the nanocrystal, and (c) in some cases the reduction of the surface site symmetry for the doping ion. Sometimes these differences can become a limitation in the nanocrystals in comparison with bulk counterpart.

Therefore, all these features have generated a new field of research for preparing nanocrystals based generally on sol−gel methods. KREW nanocrystal preparation is based on a modified Pechini Sol−Gel method, also known as the polymerized complexes method.[19,20] This chemical route is highly feasible and low cost and can be prepared at a lower temperature than single-crystal growth. The method consists of forming a polymeric resin between metal chelate complexes (formed by metallic ions and α-hydroxycarboxylic acids such as citric acid or EDTA) by heating with a polyhydroxyl alcohol such as ethylene glycol, which in turn leads to polyesterification.

In the present work, we synthesized nanocrystalline monoclinic KYbW and Er:KYbW and studied the optical spectroscopic features of Yb^{3+} and Er^{3+} in these nanocrystals and compared them with the bulk single crystal.

II. Synthesis and Experimental Techniques

A. Synthesis of Nanocrystals. A modified Pechini method was used to prepare the nanocrystals of KYbW and 50% at. Er:KYbW. Figure 1 shows the flow scheme of the synthesis procedure. First, we converted powders of K_2CO_3 (Flucka, 99%), Yb_2O_3 (Aldrich, 99.9%), Er_2O_3 (Aldrich, 99.9%), and a stoichiometric amount of ammonium paratungstate $(NH_4)_{10}W_{12}O_{41} \cdot 7H_2O$ (Riedel-de Häen, 99%) into their nitrates by dissolving them in concentrated HNO_3. Excess nitric acid was removed by slowly stirring and heating to obtain nitrate precipitates. To prepare metal−EDTA complexes, an aqueous solution with a specific molar ratio of EDTA was added to the total metal ions. This ratio (C_M) was defined as C_M = [EDTA]/[METAL] and

equal to 1. The solution was stirred to obtain the metal−EDTA complexes. Then, ethylene glycol (EG) was added in a molar ratio C_E = 2, where C_E = [EDTA]/[EG]. The resulting solution was heated to obtain the precursor resin. The following step was an initial calcination at 573 K for 3 h to start the decomposition of the precursor resin and to obtain the precursor powder. To obtain the nanocrystals, the precursor powder was calcined at 973 K for several hours. We published in previous studies and in greater detail the way in which we optimized the different experimental variables for the modified Pechini method to obtain KREW nanocrystals.[20,21]

B. Characterization Techniques. We did thermal analyses using a DTA-TG instrument (TA Instruments simultaneous differential techniques instrument SDT 2960) in air flow (90 cm^3/min) at a heating rate of 10 K/min. This allowed us to characterize the thermal decomposition of the precursor dried resin obtained by the modified Pechini method. Al_2O_3 powder was used as a reference; the weights of the sample and reference were the same.

X-ray powder diffraction patterns were performed on the powder obtained at different calcination temperatures using a D-5000 diffractometer (Bragg−Brentano parafocusing geometry) from Siemens with a $\theta-\theta$ configuration. The diffraction angle (2θ) ranged between 10° and 70°. To identify crystalline phase, the X-ray powder diffraction patterns were recorded at step size = 0.05°, step time = 3 s at room temperature. We used X-ray powder diffraction to refine the unit cell parameters of the crystal structure of the nanocrystals obtained. In these cases, the X-ray powder diffraction patterns were recorded at step size = 0.02°, step time = 16 s at room temperature. Lattice parameters were calculated using the FULLPROF program based on the Rietveld method,[22,23] where the crystalline structure obtained by X-ray single-crystal diffraction was used as the starting structural model.[24] Crystallite size L was measured using Scherrer's equation, $L = K\lambda/(\beta \cos \theta_B)$, for peak broadening from size effects only (β is the FWHM measured in radians on the 2θ scale, λ is the wavelength used, θ_B is the Bragg angle for the measured hkl peak, and K is a constant equal to 0.9 for L taken as the volume-averaged crystallite dimension perpendicular to the hkl diffraction plane).[25]

The particle homogeneity, morphology, and size distribution of nanocrystals were observed using a scanning electron microscope (JEOL JSM 6400, SEM), transmission electron microscopy (JEOL JEM-1011, TEM) with a MegaView III (Soft Imaging System), and high-resolution transmission electron microscopy (TEM 300 kV Philips CM30 with spectrophotometer Link LZ5, HRTEM). To examine the samples by TEM techniques, the nanocrystals were dispersed in ethanol (Merck, pro analysis 99.8%). Ultrasonication was used to reduce and disperse the agglomerates. Then, they were drop cast onto a copper grid covered by a porous carbon film.

To determine the chemical composition of the nanocrystals, we carried out electron probe microanalysis (EPMA) in a Cameca SX50 microprobe analyzer operating in wavelength-dispersive mode. Ytterbium and erbium were both measured using the line Lα and LiF as an analyzing crystal.

The optical absorption of the undoped KYbW and Er:KYbW nanocrystals at room temperature and 6 K was measured using a Varian Cary 500 spectrophotometer. Oxford Instruments cryostats (SU 12 model) with close-cycle helium gas flow cooled the samples for the low-temperature measurements.

The fluorescence was dispersed using a 0.46 m double monochromator (JOBIN YVON-SPEX HR 460). We excited the nanocrystals using a Ti:Sapphire laser at 933 nm. For the
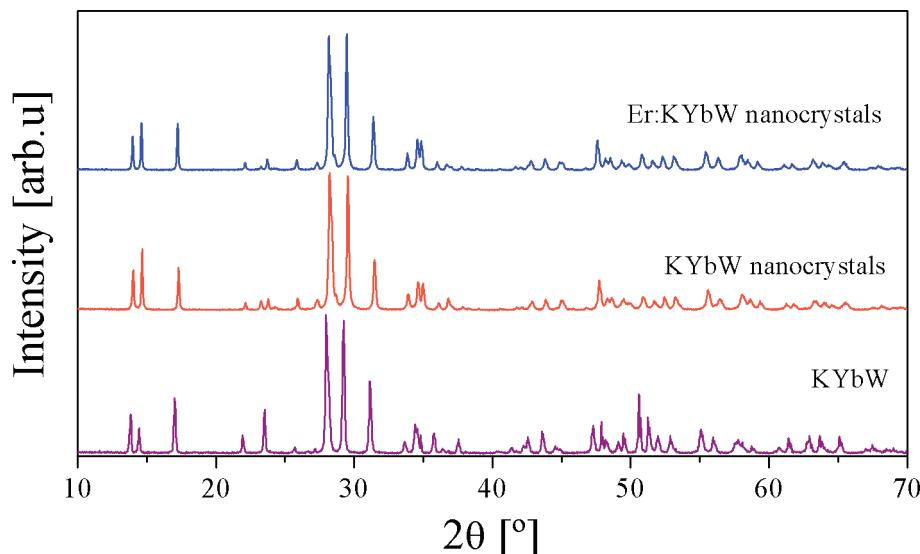
Monoclinic Er:KYb(WO$_4$)$_2$ Nanocrystals

J. Phys. Chem. C, Vol. 113, No. 35, 2009 **15499**

Figure 3. X-ray powder diffraction patterns of the KYbW and Er:KYbW nanocrystals and the bulk crystal obtained by calcination at 973K.
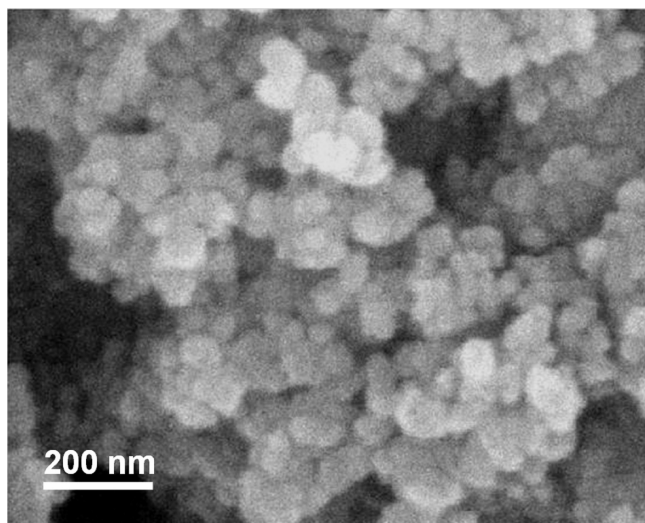

Figure 4. SEM image of the KYbW nanocrystals obtained.

detection, the infrared emission was collected at 90° using a cooled Hamamatsu R55092-72 NIR photomultiplier. It was connected to the lock-in amplifier (Perkin-Elmer DSP-7265). To work at low temperature we used a cryostat Oxford (CCC1104) with helium-gas flow, as described above for low-temperature emission measurements. All curves were measured with 2 nm spectral resolution.

Fluorescence lifetimes were excited with a Quanta-Ray MOPO-HF optical parametric oscillator. This system provides laser pulses shorter than 10 ns from 440 to 680 nm and from 730 to 1750 nm. The pulse energy were ~25 mJ for λ = 930 nm and 12 mW for λ = 1490 nm. The fluorescence was dispersed by a single-grating SPEX spectrometer (f = 34 cm) and measured by a Hamamatsu InP/InGaAs-cooled photomultiplier, model H9170-75, sensitive in the 950−1700 nm range. The electrical signals were recorded in a Tektronix oscilloscope, model TDS-520.

III. Results and Discussion

A. Thermal Analysis of the Precursor Powder. The DTA-TG thermograms of the precursor powder in the modified Pechini method are shown in Figure 2. The thermal decomposition could be divided into four steps associated with the weight loss. In the first stage (I), the temperature interval and weight loss were 300−530 K and −15%, respectively. This weight loss is related to the evaporation of water, which was formed by the esterification reaction between the EDTA and the EG. In this stage, we observed a weak endothermic peak around 517 K that can be attributed to the evaporation of the organic solvents.[26,27] In the second stage (II), the temperature interval was 530−700 K and weight loss was −40%. The exothermic peak at 660 K is associated with the oxidation of the residual organic compounds. In the next stage (III), the temperature interval was 700−800 K and weight loss was −62%. The strong exothermic peak observed at 796 K corresponds to the decomposition/combustion of the polyester and also the crystallization process because the crystallization process involves no weight loss in the TG curve but has an exothermic peak in the DTA curve. For this reason, it could be said that there are overlapping processes in this range of temperature.

In the last stage (IV) we studied the polymorphic transformation and melting point of the nanocrystals. This was also compared with the bulk single crystal. For the bulk single crystal, the two exothermic peaks at 1322 an 1327 K are attributed to the transformation phase and the crystal's melting point.[28,29] Both these processes are overlapped for the nanocrystals and there is only one peak around 1310 K. The melting point shift between the KYbW nanocrystals and the bulk single crystal was related to particle size because the smaller size of the nanocrystals affected the material thermodynamic properties.[30,31]

A process involving one possible secondary compound can generate the other endothermic peak of around 1180 K. No peak of EDTA boiling was observed, so it was totally reacted and the overall weight loss was 60−65% of the initial weight.

B. Structural Characterization. Figure 3 shows the X-ray diffraction patterns of the nanocrystals obtained, which are then compared with KYbW X-ray powder pattern. It can be observed that the powder obtained belonged to the monoclinic system, with the space group *C2/c*, which makes the phase interesting for laser applications. DTA-TG analysis shows that monoclinic KYbW nanocrystals crystallize at 796 K, whereas the diffraction peaks that correspond to the monoclinic phase do not appear clearly well defined until the precursor powder has been calcinated at 973 K.

The unit cell parameters of monoclinic KYbW and Er:KYbW nanocrystals were refined from a X-ray powder pattern at room
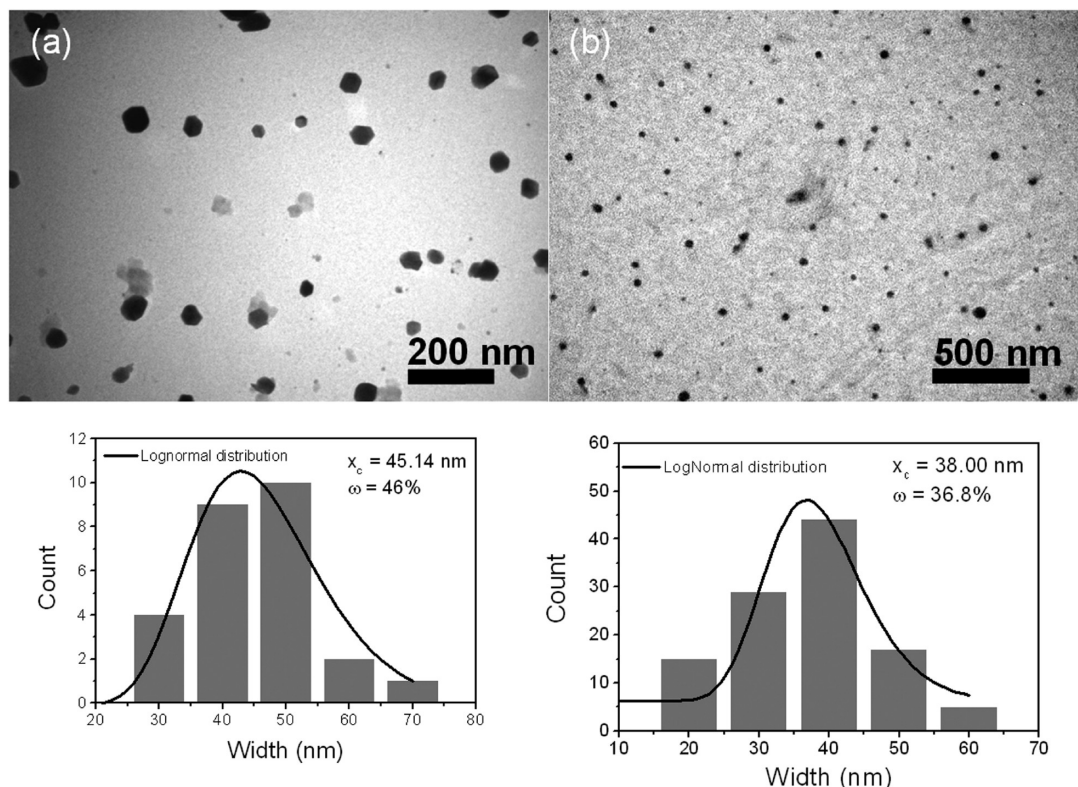
Figure 5. TEM image and particle size distribution of (a) KYbW and (b) Er:KYbW nanocrystals.
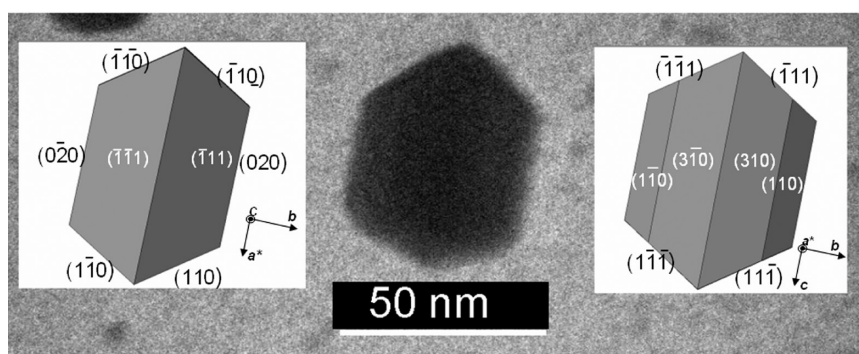

Figure 6. Detailed TEM image of a KYbW nanocrystal, and two schemes of different crystallographic orientations of KYbW habit model.
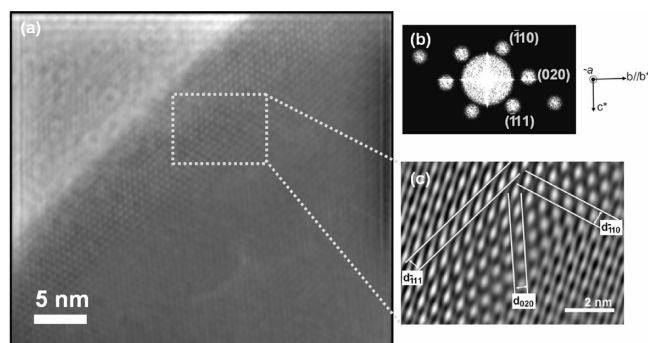

Figure 7. (a) High-resolution image of the KYbW nanocrystals. (b) FFT pattern that indicates the crystal orientation and (*hkl*) planes. (c) Laplacian filtered image of the inset selected area in the anterior image and interplanar lattice spacing $d_{\bar{1}10} = 6.3256$ Å, $d_{\bar{1}11} = 6.0474$ Å, and $d_{020} = 5.1311$ Å.

temperature. The unit cell parameters of the nanocrystals are summarized in Table 1 in comparison with the unit cell parameters of KYbW and KErW obtained by X-ray single crystal and X-ray powder diffraction. The unit cell parameters

of Er:KYbW nanocrystals are slightly larger in comparison with undoped KYbW due to erbium doping. This is because the erbium ions (ionic radius = 1.004 Å, coordination number, cn = 8) have larger ionic radium than ytterbium ions (ionic radius = 0.985 Å, cn = 8).[32] On the other hand, the unit cell parameters in the KYbW nanocrystals are similar with the previous KYbW results obtained by X-ray powder and X-ray single-crystal diffraction.

C. Morphological Characterization and Particle Size Distribution. The SEM equipment was used in order to observe the shape and size homogeneity of the nanocrystals. As can be seen in Figure 4, the particle sizes are in the 100−50 nm range.

Transmission electron microscopy was used to estimate the particle size distribution from a TEM image and the Metamorph software. Figure 5 shows two different TEM images with their respective size distribution histograms that correspond to KYbW (a) and Er:KYbW (b) nanocrystals. We treat the nanocrystals as spherical particles despite them having crystal habit shapes. For this reason, we use the width as a defining parameter for the diameter of the particle size. The particle size histograms have a log-normal distribution when the nanocrystals were

Monoclinic Er:KYb(WO₄)₂ Nanocrystals

J. Phys. Chem. C, Vol. 113, No. 35, 2009 **15501**

TABLE 1: Unit Cell Parameters of the KYbW and Er:KYbW Nanocrystals, and the X-ray Powder Diffraction and X-ray Single-Crystal Diffraction of KREW (RE = Yb, Er) as a Reference

	a (Å)	b (Å)	c (Å)	β (deg)	V (Å³)
KYbW[a 4]	10.590(4)	10.290(6)	7.478(2)	130.70(2)	617.8(5)
KYbW[b 42]	10.6003(12)	10.2973(12)	7.5066(8)	130.766(6)	618.78(12)
KYbW nanocrystals[b]	10.6026(6)	10.297(6)	7.5036(4)	130.753(3)	618.33(6)
KErW[a 43]	10.615(2)	10.316(2)	7.534(2)	130.73(3)	625.2(2)
KErW[b 43]	10.6261(13)	10.3254(14)	7.5416(8)	130.762(6)	626.73(13)
Er:KYbW nanocrystals[b]	10.6103(5)	10.2886(5)	7.5204(3)	130.75(2)	621.9(5)

[a] By X-ray single-crystal diffraction. [b] By X-ray powder diffraction.

formed by nucleation, condensation, and particle growth, as described in the literature.[33,34] In our case, the predominant particle size corresponds to 30−50 nm. For KYbW and Er:KYbW, the mean particle size and dispersion size (σ is the standard deviation of the mode and 2σ is the dispersion of the mode) were 45 nm and 46% and 38 nm and 36%, respectively. The particle sizes estimated by Scherrer's equation for KYbW and Er:KYbW nanocrystals were 47 and 42 nm, respectively. This coincided well with the size observed by TEM.

Furthermore, the TEM technique was also used to observe and characterize the habit and morphology of the nanocrystals. To characterize the habit of the nanocrystals, we draw the habit mode of KYbW using the Shape software program based on the Wulff plot. Two possible crystallographic orientations of the habit could fit to the selected nanocrystal as we show in Figure 6.[35] The forms that appeared are {1$\bar{1}$1}, {020}, {3$\bar{1}$0}, and {1$\bar{1}$0}. The appearance of these forms agrees with their large interplanar d_{hkl} and the PBCs parallel to them.[4]

Figure 7a shows the HRTEM image of the KYbW nanocrystals, in which visible lattice planes can be observed, indicating the high degree of crystallinity. The fast Fourier transform (FFT) pattern (Figure 7b) can be well indexed according to the monoclinic phase KYbW structure. With these results, we clearly observed the interplanar lattice spacing of the ($\bar{1}$10), ($\bar{1}$11), and (020) planes which are 6.3256, 6.0474, and 5.1311 Å, respectively (Figure 7c).

D. Optical Absorption. In the KYbW structure, Yb³⁺ ions are located in a unique site surrounded by eight oxygen ions forming a distorted square antiprism with C_2 symmetry.[4] Due to the fact that the ytterbium ion has an odd number of electrons, the breaking of the degeneracy is not total and Krammers doublets are generated. Trivalent erbium in Er:KYbW has the same crystal site as ytterbium. The presence of the dopant Er³⁺ in the host material (KYbW) was measured quantitatively by EPMA. The composition measured was KEr$_{0.5}$Yb$_{0.5}$(WO₄)₂ (50% at. Er:KYbW).

As mentioned in the Introduction, to excite the photoluminescence of these nanocrystals by ytterbium energy transfer to erbium, the nanocrystals must be excited by a NIR beam, around the 0.9−1.1 μm range. Figure 8 shows the room-temperature optical absorption in this range, which corresponds to the ²F$_{7/2}$ → ²F$_{5/2}$ transition for ytterbium in KYbW nanocrystals.

It is observed that the relation between the intensity peaks in the nanocrystal spectrum is similar to the optical absorption of KYbW bulk crystal averaged among the three main polarizations ($E//N_g$, $E//N_m$, and $E//N_p$). This is logical because there is a random orientation of the nanocrystals.

To determine the energy values of the ytterbium Starks sublevels, we measured the optical absorption at a low temperature of 6 K (Figure 9). At low temperature, the electronic population was in the lowest sublevel of the ground energy level, whereas at room temperature the electronic population was distributed among all the energy sublevels of the ground energy level. That is, most
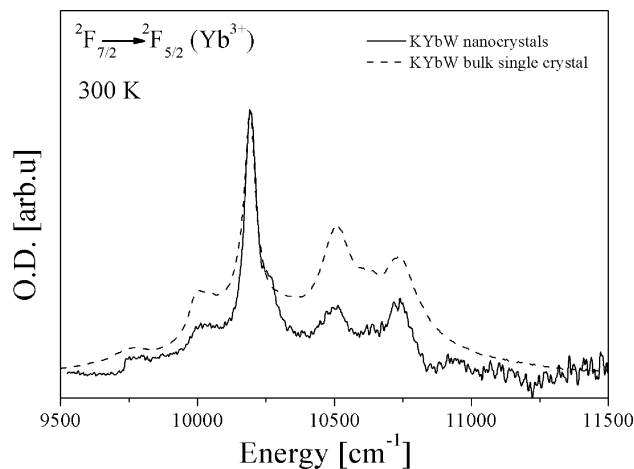

Figure 8. Optical absorption at room temperature of ytterbium in KYbW nanocrystals, compared to the polarized room-temperature absorption in a bulk single-crystal KYbW.
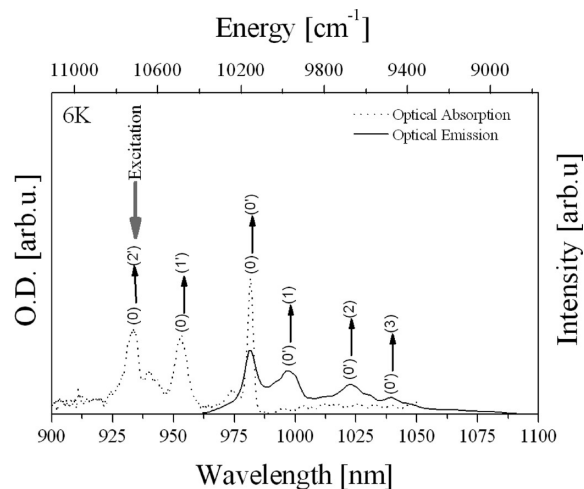

Figure 9. Optical absorption and optical emission at low temperature of trivalent ytterbium in KYbW nanocrystals.

of the energy was localized in only one transition and is more intense than room temperature, where the energy was distributed in several transitions of the ground energy levels. For this reason, when working at low temperature, it is better to study all the excited energy levels for each active ion. Figure 9 corresponds to the ²F$_{7/2}$(0) → ²F$_{5/2}$ (n'), n' = 0, 1, 2 electronic transitions, leading to the excited state ²F$_{5/2}$ sublevels values: (0') 10 186, (1') 10 493, and (2') 10 714 cm⁻¹ (Table 2).

The splitting of all excited energy levels of erbium in KYbW nanocrystals was also determined according to the Kramers levels $(2J + 1)/2$, and this is shown in Table 2. Figure 10 shows the optical absorption at 6 K in the range 376−1500 nm (6400−26 600 cm⁻¹) for the trivalent erbium. The hypersensitive transitions ⁴I$_{15/2}$ → ²H$_{11/2}$ and ⁴I$_{15/2}$ → ⁴G$_{11/2}$ show the largest

TABLE 2: Experimental Energy Levels of Er^{3+} and Yb^{3+} Ions Observed in Er:KYbW Nanocrystals and Bulk Single Crystal

|		energy (cm^{-1})	
active ion	$^{2S+1}L_J$	nanocrystals	bulk single crystal[8]
Er^{3+}	$^4I_{15/2}$	0, 25, 57, 104, 138, 241, 1 peak missing, 303	0, 25, 61, 105, 135, 237, 295, 309
	$^4I_{13/2}$	6515, 6544, 6568, 6602, 6669, 6720, 6735	6515, 6543, 6563, 6670, 6723, 6737
	$^4I_{9/2}$	not observed	12 336, 12 441, 12 468, 12 498, 12 556
	$^4F_{9/2}$	15 179, 15 204, 15 281, 15 331, 15 366	15 201, 15 280, 15 332, 15 341, 15 366
	$^4S_{3/2}$	18 310, 18 377	18 308, 18 376
	$^2H_{11/2}$	19 035, 19 056, 19 129, 19 170, 19 194, 19 219	19 035, 19 056, 19 128, 19 170, 19 205, 19 219
	$^4F_{7/2}$	20 423, 20 472, 20 497, 20 575	20 421, 20 471, 20 497, 20 573
	$^4F_{5/2}$	22 107, 22 138, 22 177	22 104, 22 136, 22 177
	$^4F_{3/2}$	22 388, 22 452	22 450, 22 551
	$^2H_{9/2}$	24 485, 24 524, 24 543, 24 571,1 peak missing	24 484, 24 523, 24 569, 24 584, 24 609
	$^4G_{11/2}$	26 205, 26 218, 26 325, 26 388, 26 437, 26 459	26 208, 26 223, 26 326, 26 386, 26 434, 26 457
Yb^{3+}	$^2F_{7/2}$	0, 152, 410, 561	0, 168, 438, 555
	$^2F_{5/2}$	10 186, 10 493, 10 714	10 187, 10 490, 10 728

oscillator strengths. Generally, in Figure 10, extra peaks appear corresponding to the transitions from some thermal population in the first excited sublevels of the ground $^4I_{15/2}$ multiplet.

E. Optical Emission. We excited Yb^{3+} at 933 nm with a Ti:Sapphire continuous laser in order to study the optical emission in the Er:KYbW nanocrystals obtained by the modified Pechini method.

Figure 9 shows the 1 μm emission of Yb^{3+} at low temperature (overlapped with low-temperature absorption). The maximum 10 186 cm^{-1} appears in the spectra for the $^2F_{5/2}(0') \rightarrow ^2F_{7/2}(0)$ transition. The position of this peak determines the energy of the $^2F_{5/2}(0')$ sublevel. The energy values of the electronic

transitions are 9625, 9776, 10 034, and 10 186 cm^{-1} and correspond to $^2F_{5/2}(0') \rightarrow ^2F_{7/2}(n)$, $n = 3, 2, 1$, and 0 electronic transitions, respectively. We determined the energy of the Stark sublevels of the ground state $^2F_{7/2}$: (0) 0, (1) 152, (2) 410, and (3) 561 cm^{-1}. Having now determined the splitting of the ground state we can state that at room temperature (300 K) only 3.95% of the ions are in the $^2F_{7/2}$ (3) sublevel.

Of particular note is the broadening of the peaks in the nanocrystals compared to the bulk counterpart, which has been reported in other studies.[36] This fact can be attributed to contamination by adsorbed atmospheric CO_2 and H_2O or to contamination adsorbed in the last step of the synthesis process
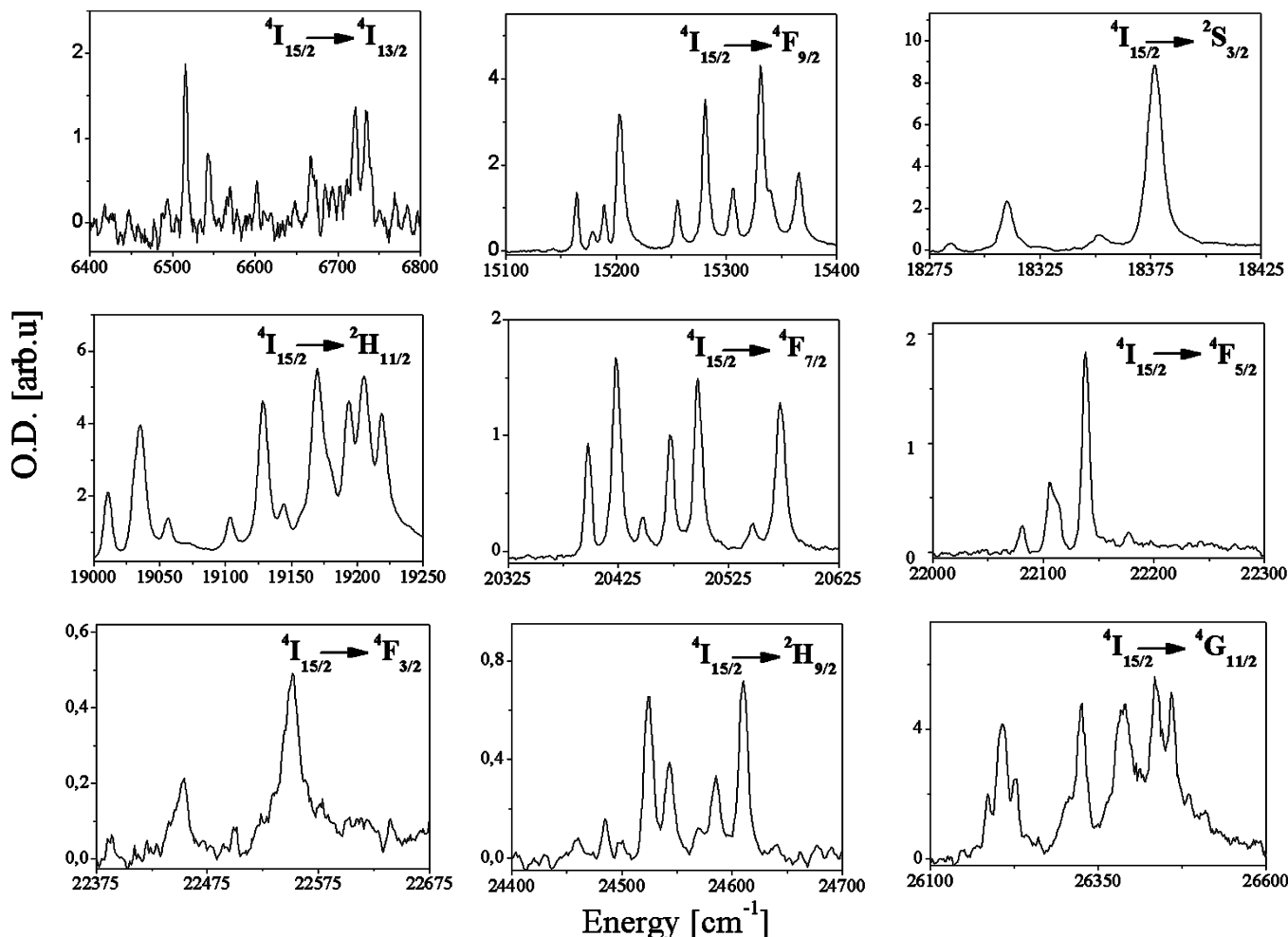
Figure 10. Optical absorption at low temperature of erbium in KYbW nanocrystals in the 376−1500 nm range.
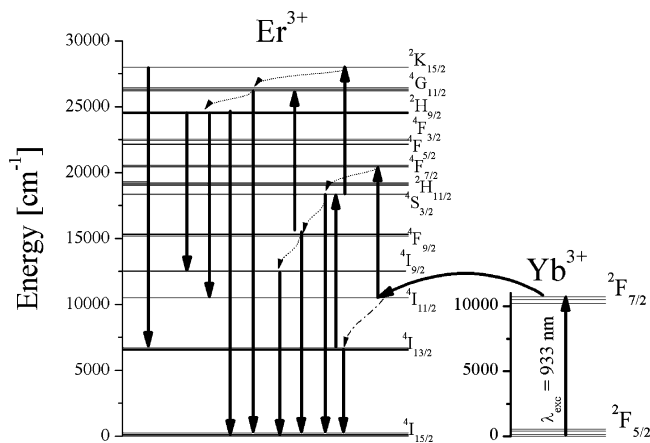
Monoclinic Er:KYb(WO$_4$)$_2$ Nanocrystals

J. Phys. Chem. C, Vol. 113, No. 35, 2009 **15503**

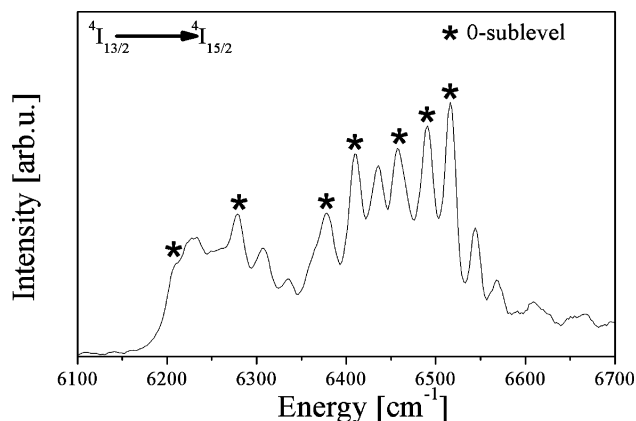**Figure 11.** Energy-level diagram and diagram of ytterbium and erbium emissions.

Figure 12. Optical emission at 6 K of erbium in KYbW nanocrystals of the $^4I_{13/2} \rightarrow {}^4I_{15/2}$ transition after pumping at 933 nm by Ti:Sapphire laser excitation.

where these compounds are a byproduct of the combustion process on the surface of the nanocrystals.[37] The adsorbed surface ions would give rise to a broader emission profile, and thus, the luminescence spectrum of the doped nanocrystals would be more homogeneously broadened compared with the emission spectrum of the Yb^{3+} in the bulk single-crystal material.[38] We reported the infrared spectrum of the nanocrystalline KYbW during its synthesis in a previous paper,[21] where we showed bands at 1640 cm^{-1} attributed to hydroxyl groups (O−H) and bands at 1726, 1400, and 1200 cm^{-1} attributed to the carboxylic groups (−COO−). The bands at 1520 and 1400 cm^{-1}, which disappeared during the calcinations, were assigned to the ionized carboxylates and carbonates. Consequently, the presence of these large vibrational quanta in the nanocrystals makes multiphonon relaxation much more probable than in single bulk crystals (maximum phonon energy of KYbW nanocrystals = 908 cm^{-1}).[20]

Another interesting infrared emission is the one related to the erbium $^4I_{13/2} \rightarrow {}^4I_{15/2}$ transition, located in the range of 1.55 μm. After selective Yb^{3+} excitation at 933 nm, the electrons of the excited energy level ($^2F_{5/2}$, Yb^{3+}) decay radiatively to the ground state or transfer part of their energy to $^4I_{11/2}$ (Er^{3+}). This is due to the good energetic overlap between these two levels. There is then a very fast nonradiative decay from $^4I_{11/2}$ to $^4I_{13/2}$ erbium energy levels. The radiative decay to the ground state ($^4I_{15/2}$) takes place late in the process. Figure 11 shows the energy transfer mechanism.

This optical emission at low temperature is used to determine the splitting of the erbium ground state $^4I_{15/2}$ (Figure 12). From the energy values corresponding to the $^4I_{13/2}$ sublevels obtained by optical absorption at low temperature, we determined the splitting of the ground state of erbium: 0, 25, 57, 104, 138, 241, and 303 cm^{-1}. The energy values attributed to the $^4I_{13/2}$ (0') $\rightarrow {}^4I_{15/2}$ (6) and $^4I_{13/2}$ (0') $\rightarrow {}^4I_{15/2}$ (7) transitions are overlapped. For this reason, the values of the $^4I_{15/2}$ (6) and $^4I_{15/2}$ (7) sublevels cannot be determined.

Figure 13 shows the 6 K emission in the ultraviolet and visible regions (357−830 nm) of Er:KYbW nanocrystals under excitation in the Yb^{3+} $^2F_{5/2}$ multiplet. The broad band signals correspond to $^4G_{11/2} \rightarrow {}^4I_{15/2}$, $^2H_{9/2} \rightarrow {}^4I_{15/2}$, $^2K_{15/2} \rightarrow {}^4I_{13/2}$, $^4S_{3/2} \rightarrow {}^4I_{15/2}$, $^4F_{9/2} \rightarrow {}^4I_{15/2}$, $^2H_{9/2} \rightarrow {}^4I_{11/2}$, $^4I_{9/2} \rightarrow {}^4I_{15/2}$, and $^2H_{9/2} \rightarrow {}^4I_{9/2}$ transitions.

When generating all the emissions, the excited electrons of ytterbium in the $^2F_{5/2}$ level decay radiatively to the ground state or transfer part of their energy to the $^4I_{11/2}$ energy level of erbium. The electrons in the $^4I_{11/2}$ level consistently increase their energy to the $^4F_{7/2}$ level, and a very fast nonradiative relaxation took place to the $^4S_{3/2}$ level, where the emission $^4S_{3/2} \rightarrow {}^4I_{15/2}$ takes place around 552 nm. $^4S_{3/2}$ can be populated also by direct reabsorption of the excited state $^4I_{13/2}$. From the $^4S_{3/2}$ level to $^4F_{9/2}$, a nonradiative relaxation takes place and generates an emission of around 669 nm ($^4F_{9/2} \rightarrow {}^4I_{15/2}$). From $^4F_{9/2}$ to $^4I_{9/2}$, a nonradiative relaxation takes place and generates an emission of around 801 nm ($^4I_{9/2} \rightarrow {}^4I_{15/2}$). On the other hand, if the cross-relaxation mechanism from $^4S_{3/2}$ allows the $^2K_{15/2}$ level population of erbium, new emission bands are generated. From $^2K_{15/2}$, around 471 nm $^2K_{15/2} \rightarrow {}^4I_{13/2}$ is emitted. From $^2K_{15/2}$, there is a nonradiative relaxation to $^4G_{11/2}$ generating the emission $^4G_{11/2} \rightarrow {}^4I_{15/2}$ around 382 nm. Some electron population in the $^4G_{11/2}$ state is also coming from the excited-state absorption of $^4F_{9/2}$, being $^4F_{9/2} \rightarrow {}^4G_{11/2}$, which is nearly resonant to the excitation wavelength. $^2H_{9/2} \rightarrow {}^4I_{15/2}$ around 403 nm, $^2H_{9/2} \rightarrow {}^4I_{11/2}$ around 696 nm, and $^2H_{9/2} \rightarrow {}^4I_{9/2}$ around 813 nm are generated from $^4G_{11/2}$ via the nonradiative relaxation to populate the $^2H_{9/2}$ level.

We studied the up-conversion mechanism in green luminescence ($^4S_{3/2} \rightarrow {}^4I_{15/2}$). To verify this mechanism, we measured the ratio between the intensity of the green luminescence and the intensity of infrared excitation at room temperature. The relationship between the exciting power intensity and the fluorescence intensity can be described as $I_{green} \propto I_{IR}{}^n$, where I_{green} is the green output intensity, (I_{IR}) is the exciting power intensity, and n is the number of IR photons absorbed per visible photon emitted.[39] The value of n in the linear slope of the logarithmic representation of I_{IR} with regard to I_{green} is around 1.5; this fact indicates that two photons are involved in the up-conversion mechanism (see inset in Figure 13).

F. Lifetime Measurements. We studied the decay kinetics of the ytterbium ($^2F_{5/2} \rightarrow {}^2F_{7/2}$) transition at 1025 nm and the erbium ($^4I_{13/2} \rightarrow {}^4I_{15/2}$) transition at 1533 nm. Some emission reabsorption is expected in both cases because the transitions reach the electronically populated (at room temperature) ground state. This effect is expected to be particularly important in the samples presently analyzed, because of the very high concentration of ytterbium and erbium. To minimize reabsorption effects we performed lifetime measurements on KYbW and Er:KYbW nanocrystals dispersed in ethylene glycol inside quartz cells. None of the light decays obtained were single exponential, due to the presence of resonant energy transfer between Yb−Yb,
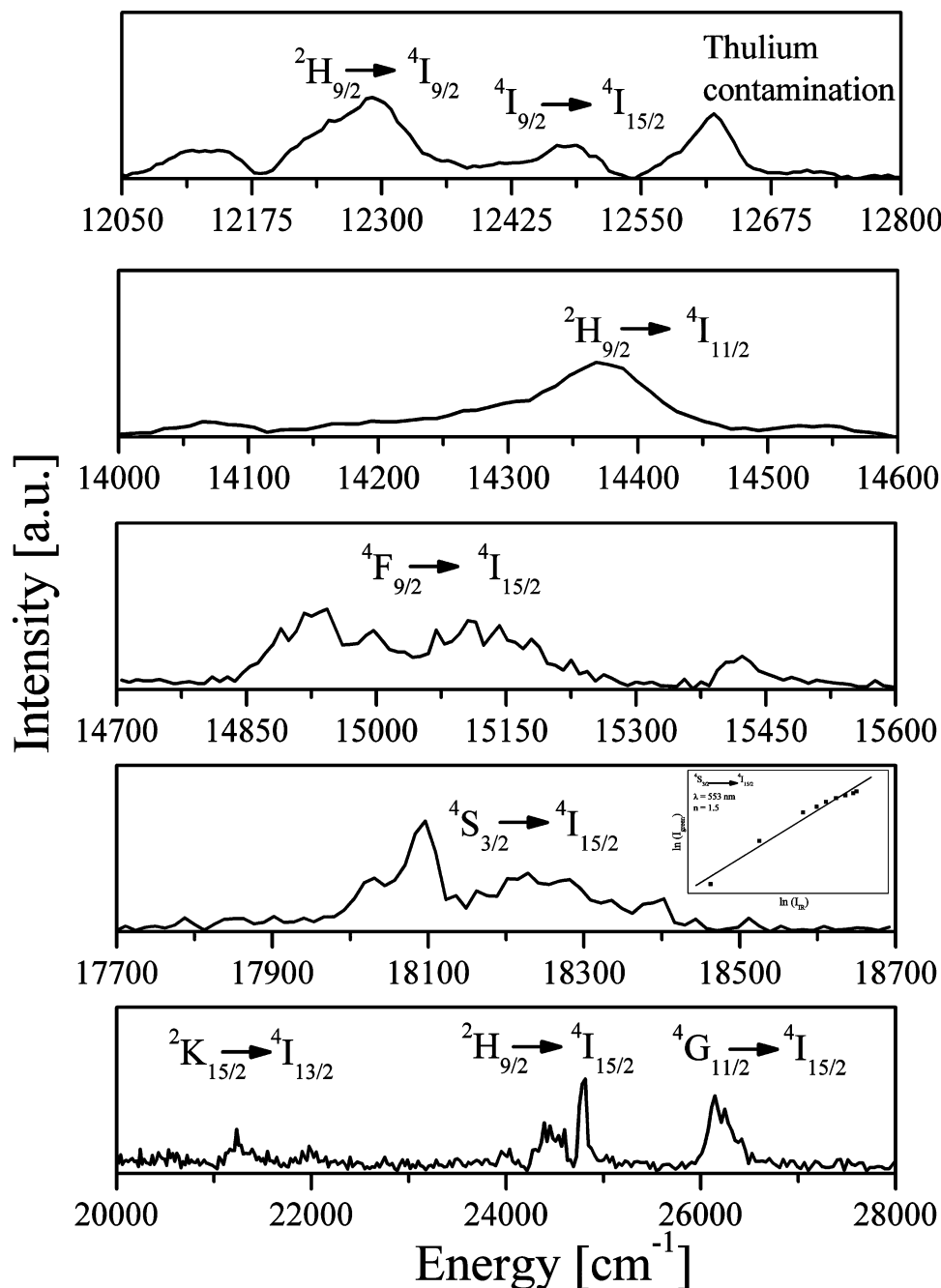
Figure 13. Optical emission at 6 K of the 350−830 nm range after pumping at 933 nm by Ti:Sapphire laser excitation.

Yb−Er, and Er−Er ions. This situation is described by the Inokuti−Hirayama model[40]

$$I(t) = I(0)\exp\left[\frac{-t}{\tau_0} - \Gamma\left(1 - \frac{3}{s}\right)\frac{[N]}{c_0}\left(\frac{t}{\tau_0}\right)^{3/s}\right] \quad (1)$$

where $c_0 = 3/4\pi R_c^3$ is a critical concentration related to the distance R_c at which the donor−acceptor energy transfer rate equals the spontaneous decay rate. $[N]$ is the concentration of acceptors. τ_0 is the lifetime in the absence of energy transfer. $\Gamma(x)$ is the gamma function, and $s = 6$, 8, or 10 describes the nature of the transfer mechanism, i.e., electric dipole−dipole, dipole−quadrupole, or quadrupole−quadrupole, respectively.

Figure 14 shows the $t/\tau_0 + \ln[I(t)/I(0)]$ versus $t^{3/s}$ representations of the three cases considered. A linear behavior was only

obtained for $s = 6$ in all cases. We first analyzed the Yb^{3+} ($^2F_{5/2} \rightarrow {}^2F_{7/2}$) decay exciting at $\lambda = 930$ nm and monitoring the emission at $\lambda = 1025$ nm. The above-mentioned representation for the Yb decay in KYbW nanocrystals showed a clear departure from the linearity when we use the Yb concentration as the acceptor concentration, $[Yb] = 6.4 \times 10^{21}$ cm^{-3}, and the lifetime of bulk KYbW single crystals, $\tau_0 = 270$ μs.[6] The linear behavior shown in Figure 14a was obtained using a shorter lifetime, namely, $\tau_0 = 110$ μs. However, in the Er:KYbW nanocrystals the linear behavior shown in Figure 14b was obtained using the value properties of Yb in bulk crystals. Therefore, the Yb lifetime reduction observed in KYbW nanocrystals should be associated to a specific feature of these nanocrystals rather than to an intrinsic property of the Yb ion. The decay times of fluorescence ions in nanocrystals are often shorter than in bulk crystals, because of nonradiative processes
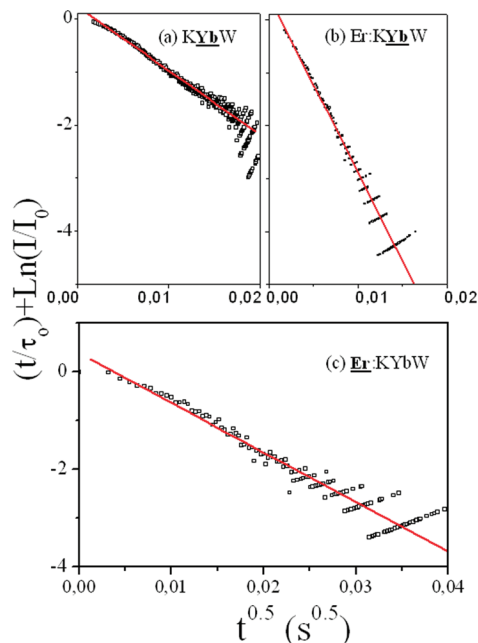
Monoclinic Er:KYb(WO₄)₂ Nanocrystals

J. Phys. Chem. C, Vol. 113, No. 35, 2009 **15505**

Figure 14. Representations of the Inokuti−Hirayama model for fluorescence decay curves. (a) $^2F_{5/2} \rightarrow {}^2F_{7/2}$ (Yb^{3+}) transition in KYbW nanocrystals. (b) $^2F_{5/2} \rightarrow {}^2F_{7/2}$ (Yb^{3+}) transition in Er:KYbW nanocrystals. (c) $^4I_{13/2} \rightarrow {}^4I_{15/2}$ (Er^{3+}) transition in Er:KYbW nanocrystals.

associated to contaminants on their surface, for instance, adsorbed atmospheric CO_2 and H_2O or contaminants adsorbed in the last step of the synthesis where these compounds are byproduct of the combustion process.[41] The critical distance R_c obtained for the Yb−Yb transfer in KYbW was 3.0 nm, and the distance obtained for the transfer from Yb to Yb and Er ions in Er:KYbW nanocrystals was 4.9 nm. This result is consistent with a higher probability of Yb−Er transfer than for Yb−Yb processes.

Figure 14c shows the $t/\tau_0 + \ln[I(t)/I(0)]$ versus $t^{3/s}$ representation of the $^4I_{13/2} \rightarrow {}^4I_{15/2}$ (Er^{3+}) decay in the Er:KYbW nanocrystals. The transition was excited at $\lambda = 1490$ nm, and the emission was monitored at $\lambda = 1533$ nm. A good linear fit was obtained using the lifetime properties of Er^{3+} in bulk crystals, $\tau_0 = 1$ ms. In that case the critical distance R_c obtained for the Er−Er and Er−Yb transfer was 4.1 nm.

IV. Conclusions

Nanocrystals with a mean particle size and dispersion size of 45 nm and 46% for KYbW and 38 nm and 36% for KYb$_{0.5}$Er$_{0.5}$W have been prepared by nucleation, condensation, and particle growth by following a modified Pechini method. These nanocrystals have the monoclinic $C2/c$ phase, and the unit cell parameters refined from X-ray diffraction patterns are close to those of single crystals. Correspondingly, the Yb and Er energy level sequences of nanocrystals single crystal are very similar. They are ascribed to optically active ions in a C_2 unique symmetry site. Despite that the high concentration of active ions in the nanocrystals studied favoring energy transfer mechanisms, the analysis of the decay kinetics of $^2F_{5/2}$ Yb and $^4I_{13/2}$ Er levels reveals that they are similar to single crystals with the same levels of impurities. These nanocrystals seem therefore promising precursors for highly efficient luminescence and laser ceramics.

References and Notes

(1) Majchrowski, A.; Borowiec, M. T.; Michalski, E.; Zmija, J.; Dyakonov, V.; Szymczak, H.; Zayarnyuk, T.; Baranski, M. *Cryst. Res. Technol.* **2001**, *36*, 283.

(2) Kaminskii, A. A.; Pavlyuk, A. A.; Butaeva, T. I.; Bobovich, L. I.; Lyubchenco, V. V. *Neorg. Mater.* **1979**, *15*, 541.

(3) Borowiec, M. T.; Dyakonov, V.; Fita, I.; Nabialek, A.; Pavlyuk, A.; Szewczyk, A.; Zaleski, M.; Zubov, E. *Cryst. Res. Technol.* **1999**, *195*, 119.

(4) Pujol, M. C.; Solé, R.; Massons, J.; Gavaldà, J.; Solans, X.; Díaz, F.; Aguiló, M. *J. Appl. Crystallogr.* **2002**, *35*, 108.

(5) Klopp, P.; Griebner, U.; Petrov, V.; Mateos, X.; Bursukova, M. A.; Pujol, M. C.; Solé, R.; Gavaldà, J.; Aguiló, M.; Güell, F.; Massons, J.; Kirilov, T.; Díaz, F. *Appl. Phys. B: Laser Opt.* **2002**, *74*, 185.

(6) Pujol, M. C.; Bursukova, M.; Güell, F.; Mateos, X.; Solé, R.; Gavaldà, J.; Aguiló, M.; Massons, J.; Díaz, F.; Klopp, P.; Griebner, U.; Petrov, P. *Phys. Rev. B* **2002**, *65*, 165121.

(7) Mateos, X.; Pujol, M. C.; Güell, F.; Solé, R.; Gavaldà, J.; Aguiló, M.; Díaz, F.; Massons, J. *Phys. Rev. B* **2002**, *66*, 214104.

(8) Mateos, X.; Güell, F.; Pujol, M. C.; Bursukova, M. A.; Solé, R.; Gavaldà, J.; Aguiló, M.; Díaz, F.; Massons, J. *Appl. Phys. Lett.* **2002**, *80*, 4510.

(9) Deloach, L. D.; Payne, S. A.; Chase, L. L.; Smith, L. K.; Kway, W. L.; Krupe, W. F. *IEEE J. Quantum Electron.* **1993**, *29*, 1179.

(10) Krupe, W. F.; IEEE, J. *Sel. Top. Quantum Electron.* **2000**, *6*, 1287.

(11) Zou, X.; Toratani, H. *Phys. Rev. B* **1995**, *52*, 15889.

(12) Auzel, F. E. *Proc. IEEE* **1973**, *61*, 758.

(13) Liu, C.; Wang, X.; Jiang, Y.; Wang, Y.; Hao, S. *Rare Met.* **2006**, *25*, 471.

(14) Hreniak, D.; Strek, W.; Mazur, P.; Pazik, R.; Zabkowska-Waclawek, M. *Opt. Mater.* **2004**, *26*, 117.

(15) Meltzer, R. S.; Feofilov, S. P.; Tissue, B.; Yuan, H. B. *Phys. Rev. B* **1999**, *60*, R14012.

(16) Vetrone, F. J. *Appl. Phys.* **2004**, *96*, 19.

(17) Shalaev, V. M.; Safonov, V. P.; Poliakov, E. Y.; Markel, V. A.; Sarychev, A. K. *Fractal Surface Enhanced Optical Nonlinearities Fractal Surface Enhanced Optical Nonlinearities*; ACS Symposium Series 697; American Chemical Society: Washinton, DC, 1997.

(18) Hong, K. S.; Meltzer, R. S.; Bihari, B.; Williamns, D. K.; Tissue, B. M. *J. Lumin.* **1998**, *76−77*, 234.

(19) Pechini, M. P. U.S. Patent 3330697, 1967.

(20) Galceran, M.; Pujol, M. C.; Aguiló, M.; Díaz, F. *J. Sol-Gel Sci. Technol.* **2007**, *42*, 79.

(21) Galceran, M.; Pujol, M. C.; Méndez, C.; García, A.; Moreno, P.; Roso, L.; Aguiló, M.; Díaz, F. *J. Nanopart. Res.*; DOI: 10.1007/s11051-008-9375-2.

(22) Rodriguez-Carvajal, J. *Reference guide for the computer program Fullprof*; Laboratoire León Brillouin, EA-CNRS Saclay: France, 2000.

(23) Rietveld, H. M. *J. Appl. Crystallogr.* **1969**, *2*, 65.

(24) Pujol, M. C.; Solé, R.; Massons, J.; Gavaldà, J.; Solans, X.; Zaldo, C.; Díaz, F.; Aguiló, M. *J. Appl. Crystallogr.* **2001**, *34*, 1.

(25) Cullity, B. D. *Element of X-Ray Diffraction*; Addison-Wesley: New York, 1978.

(26) Interrante, L. V.; Jiang, Z.; Parking, D. J. *ACS Symp. Ser.* **1998**, *77*, 168.

(27) Tai, L. W.; Lessing, P. A. *J. Mater. Res.* **1992**, *7*, 502.

(28) Klevtsov, P. V.; Kozeeva, L. P.; Kharchenko, L. Y. *Sov. Phys. Crystallogr* **1974**, *2−0*, 732.

(29) Klevtsov, P. V.; Kozeeva, L. P.; Kharchenko, L. Y.; Pavlyuk, A. A. *Sov. Phys. Crystallogr.* **1974**, *19*, 342.

(30) Jiang, Q.; Zhang, Z.; Hsu, D. T.; Tong, H. Y.; Iskandar, M. *J. Mater. Sci.* **1999**, *34*, 5919.

(31) Xu, Q.; Sharp, I. D.; Yuan, C. W.; Yi, D. O.; Liao, C. Y.; Glaeser, A. M.; Minor, A. M.; Beeman, J. W.; Ridway, M. C.; Kluth, P.; Ager, J. A., III; Chrzan, D. C.; Haller, E. E. *Phys. Rev. Lett.* **2006**, *97*, 15701.

(32) Shannon, R. D. *Acta Crystallogr. A* **1976**, *32*, 751.

(33) Granqvist, C. G.; Buhrman, R. A. *J. Appl. Phys.* **1976**, *47*, 2200.

(34) Söderlund, J.; Kiss, L. B.; Niklasson, G.; Granqvist, G. G. *Phys. Rev. Lett.* **1998**, *80*, 2386.

(35) Dowty, E. *Shape for windows*, version 5.0.1; 1995.

(36) Williams, D. K.; Yuan, H.; Tissue, B. M. *J. Lumin.* **1999**, *83−84*, 297.

(37) Vetrone, F.; Boyer, J. C.; Capobianco, J. A. *J. Phys. Chem B* **2002**, *106*, 5622.

(38) Liu, G. K.; Zhuang, H. Z.; Chen, H. Y. *Nano Lett.* **2002**, *2*, 535.

(39) Pollnau, M.; Gamelin, D. R.; Lüthi, S. R.; Güdel, H. U. *Phys. Rev. B* **2000**, *61*, 3337.

(40) Inokuti, M.; Hirayama, F. *J. Chem. Phys.* **1965**, *43*, 1978.

(41) Vetrone, F.; Boyer, J. C.; Capobianco, J. A. *J. Phys. Chem B* **2002**, *106*, 5622.

(42) Pujol, M. C.; Mateos, X.; Solé, R.; Massons, J.; Gavaldà, J.; Díaz, F.; Aguiló, M. *Mater. Sci. Forum* **2001**, *710*, 378.

(43) Borowiec, M. T.; Dyakonov, V. P.; Wózniak, K.; Dobrzycki, Ł. L.; Berkowski, M.; Zubov, E. E.; Michalski, E.; Szewczyk, A.; Gutowska, M. U.; Zayarnyuk, T.; Szymczak, H. *J. Phys.: Condens. Matter* **2007**, *19*, 056206.